Determination of the spin Hall effect and the spin diffusion length of Pt from self-consistent fitting of damping enhancement and inverse spin-orbit torque measurements

Andrew J. Berger,[1] Eric R. J. Edwards,[1] Hans T. Nembach,[1] Olof Karis,[2] Mathias Weiler,[3,4] and T. J. Silva[1,*]

[1]*Quantum Electromagnetics Division, National Institute of Standards and Technology, Boulder, 80305 Colorado, USA*

[2]*Department of Physics and Astronomy, Uppsala University, Box 530, 751 20 Uppsala, Sweden*

[3]*Walther-Meißner-Institut, Bayerische Akademie der Wissenschaften , 85748 Garching, Germany*

[4]*Physik-Department, Technische Universität München, 85748 Garching, Germany*

(Received 21 November 2017; revised manuscript received 12 May 2018; published 3 July 2018)

Understanding the evolution of spin-orbit torque (SOT) with increasing heavy-metal thickness in ferromagnet/normal metal (FM/NM) bilayers is critical for the development of magnetic memory based on SOT. However, several experiments have revealed an apparent discrepancy between damping enhancement and dampinglike SOT regarding their dependence on NM thickness. Here, using linewidth and phase-resolved amplitude analysis of vector network analyzer ferromagnetic resonance (VNA-FMR) measurements, we simultaneously extract damping enhancement and both fieldlike and dampinglike inverse SOT in $Ni_{80}Fe_{20}$/Pt bilayers as a function of Pt thickness. By enforcing an interpretation of the data which satisfies Onsager reciprocity, we find that both the damping enhancement and dampinglike inverse SOT can be described by a single spin diffusion length ($\approx$4 nm), and that we can separate the spin pumping and spin-memory loss contributions to the total damping. This analysis indicates that less than 40% of the angular momentum pumped by FMR through the $Ni_{80}Fe_{20}$/Pt interface is transported as spin current into the Pt. On account of the spin-memory loss and corresponding reduction in total spin current available for spin-charge transduction in the Pt, we determine the Pt spin Hall conductivity [$\sigma_{SH} = (2.36 \pm 0.04) \times 10^6\ \omega^{-1}\,m^{-1}$] and bulk spin Hall angle ($\theta_{SH} = 0.387 \pm 0.008$) to be larger than commonly cited values. These results suggest that Pt can be an extremely useful source of SOT if the FM/NM interface can be engineered to minimize spin loss. Lastly, we find that self-consistent fitting of the damping and SOT data is best achieved by a model with Elliott-Yafet spin relaxation and extrinsic inverse spin Hall effect, such that both the spin diffusion length and spin Hall conductivity are proportional to the Pt charge conductivity.

DOI: 10.1103/PhysRevB.98.024402

I. INTRODUCTION

The use of nonmagnetic metals with strong spin-orbit coupling (SOC) to generate pure spin currents via spin-orbit effects is currently an area of intense focus, driven largely by the promise of efficient electrically controllable magnetic memory. For this application, the spin current or spin accumulation generated by SOC in a nonmagnetic layer can be used to exert a torque on an adjacent ferromagnetic (FM) layer—so-called spin-orbit torque (SOT)—in order to excite magnetization dynamics or cause switching. Central to this field of study is proper characterization of the spin-to-charge conversion that occurs in heavy-metal films such as Pt, Ta, W, and Au. There are many techniques for measuring this conversion, including ferromagnetic resonance (FMR) spin pumping [1], nonlocal spin valves [2,3], thermal spin injection via the spin Seebeck effect [4], spin Hall magnetoresistance [5], spin torque FMR [6], and harmonic analysis of Hall effect voltage measurements [7]. Several groups, using various techniques [8–12], have uncovered a discrepancy when comparing the excess damping and the spin-to-charge conversion by inverse spin Hall effect (iSHE) contributed by the normal metal (NM) layer. Specifically, the FM damping exhibits a steep increase with the introduction of only a very thin (<2 nm) NM film [13–15]. Meanwhile, the measured SOT, characterized by either spin-to-charge conversion via dc iSHE or harmonic Hall technique, develops over a much longer, length scale [16,17]. Magneto-optical measurements also demonstrate an interfacial spin accumulation in Pt due to SHE with a spin diffusion length of about 10 nm [18].

Spin-memory loss (SML) [10,19,20] and proximity-induced magnetic moments at the FM/NM interface [15] have been invoked to explain the large damping enhancement caused by thin NM films even when the NM thickness is less than its spin diffusion length. In this model, spin loss at the FM/NM interface acts as an additional parallel spin-relaxation pathway to that of spin pumping and diffusion into the Pt bulk. From damping measurements alone, the relative contributions of these mechanisms are not resolvable. In this work, we show that a self-consistent fit of Gilbert damping and dampinglike inverse spin-orbit torque (iSOT) vs Pt thickness—where both sets of data are described by the same spin diffusion length λ_s—makes it possible to separate these sources of damping. Furthermore, this data analysis methodology allows for unambiguous determination of the spin-mixing conductance $G^{\uparrow\downarrow}$ at the FM/NM interface. We therefore can ascertain the spin Hall conductivity (or spin Hall

*thomas.silva@nist.gov

angle) without having to refer to spin transport parameters $G^{\uparrow\downarrow}$ and λ_s determined from measurements performed on dissimilar samples or theoretical idealized values. For our samples of Pt deposited on $Ni_{80}Fe_{20}$[or Permalloy (Py)], only $37 \pm 6\%$ of the total damping enhancement from the Pt film is attributable to spin pumping into the Pt layer when $d_{Pt} \gg \lambda_s$.

II. EXPERIMENTAL TECHNIQUE

The data presented in this work are based on the spectroscopic and complex amplitude information encoded in FMR spectra collected with a vector network analyzer (VNA), which yield a measure of the damping and SOT, respectively. FMR damping extracted from a spectral linewidth analysis [21] has been used extensively to study the damping enhancement due to the spin pumping effect into an NM adjacent to the FM layer [22–25]. If such spectra are measured inductively with phase-sensitive VNA-FMR, it is also possible to analyze the phase and amplitude information of those spectra to quantitatively extract the fieldlike (FL) and dampinglike (DL) SOT conductivities, as we have previously described [26]. These conductivities, σ_{FL}^{SOT} and σ_{DL}^{SOT}, relate the ac charge currents produced in the NM layer via iSHE or inverse Rashba-Edelstein effect (iREE) in response to driven magnetization dynamics in the FM layer. Direct coupling to the magnetization dynamics via Faraday's law also drives ac charge currents in the NM layer, quantified by σ_{FL}^{F}. The superposition of these charge currents presents a complex inductive load to the microwave coplanar waveguide (CPW) used in VNA-FMR measurements, altering the amplitude and phase of the transmitted microwave signal, as is evident in Fig. 1, which shows VNA-FMR spectra for two samples used in this study. As described in detail in Ref. [26], ΔS_{21} represents the microwave transmission measurements normalized by their self-determined complex background signal to account for the nonresonant frequency-dependent transmission of the microwave setup. This normalization permits quantitative extraction of the resonant contributions to the sample inductance, including the spin-to-charge conversion processes in the multilayer. By Onsager reciprocity, σ_{FL}^{SOT} and σ_{DL}^{SOT} measured inductively via inverse spin-charge conversion processes are equivalent to the spin torque efficiency per unit applied electric field used by Nguyen *et al.* in Ref. [17] to describe the forward SOT process [26].

Samples

To study the Pt-thickness dependence of damping and dampinglike iSOT, we prepared two sample sets, with sputter-deposited metal multilayers consisting of substrate/Ta(1.5)/Py(d_{Py})/Pt(d_{Pt})/Ta(3), where thicknesses are indicated in nanometers and are calibrated with x-ray reflectivity measurements. In the first sample set, the thickness d_{Py} was varied from 1.5 to 10 nm while $d_{Pt} = 6$ nm was fixed. In the second set, the thickness d_{Pt} was varied from 2 to 20 nm with fixed $d_{Py} = 3.5$ nm. For each sample, an identical control sample was prepared, where Pt is substituted with Cu. The Cu thicknesses were chosen to match the sheet resistance of the corresponding Pt layer, so as to control for Faraday-effect-induced currents in the NM layer.

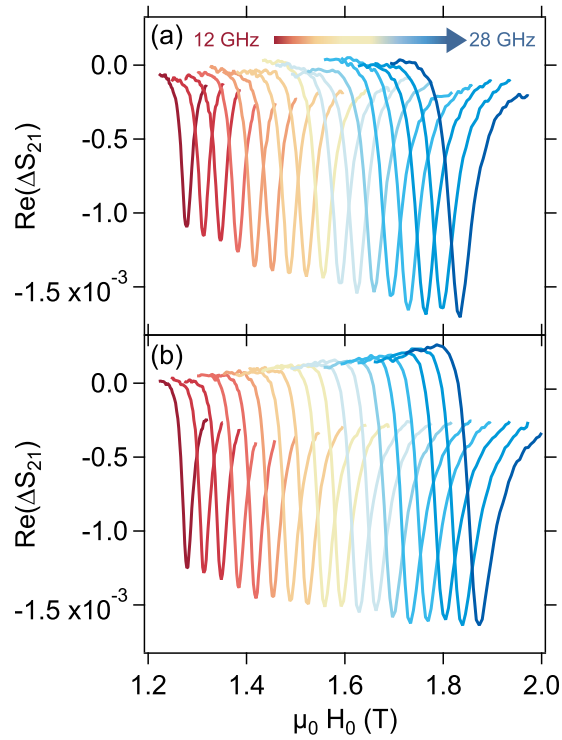

FIG. 1. VNA-FMR spectra collected as prescribed in Ref [26]. (a) Example Re(ΔS_{21}) data, collected at various excitation frequencies, for the Py(3.5)/Pt(2) sample (thicknesses in nanometers). (b) Same as (a), but for the Py(3.5)/Pt(10) sample. The imaginary signal (antisymmetric Lorentzian line shape) is more evident than in (a) due to a stronger dampinglike SOT conductivity σ_{DL}^{SOT} on account of the thicker Pt.

III. RESULTS AND DISCUSSION

A. Py thickness series

From the Py thickness series we focus on three quantities: (1) the FM contribution to the sample inductance (L_{FM}, as in Ref. [26]), (2) the effective magnetization M_{eff}, and (3) the Gilbert damping parameter α. From L_{FM} as a function of Py thickness (Fig. 2), we are able to extract the dead

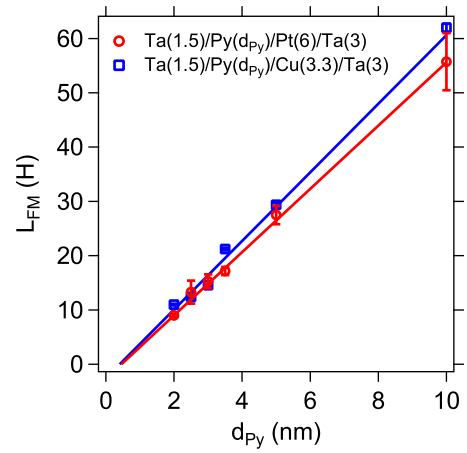

FIG. 2. Py-thickness-dependent zero-frequency inductance for both Py/Pt and Py/Cu control samples.

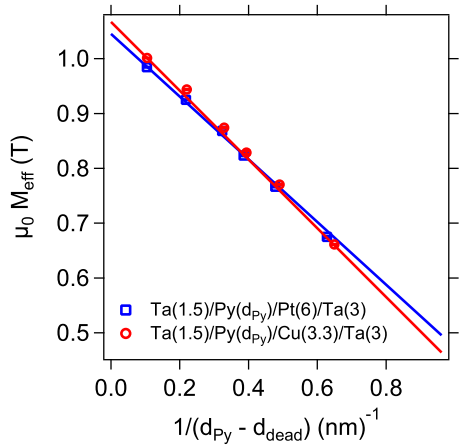

FIG. 3. M_{eff} vs inverse effective FM thickness ($d_{\text{Py}} - d_{\text{dead}}$) for Py($d_{\text{Py}}$)/Pt(6) and Py($d_{\text{Py}}$)/Cu(3.3). Dead layer thickness is determined from Fig. 2.

layer thickness, and therefore determine the effective magnetic thickness of the FM layer. From M_{eff}, we are able to determine the saturation magnetization M_{s} (Fig. 3). Lastly, from the Gilbert damping as a function of Py thickness, we can separate the intrinsic and interfacial contributions to α (Fig. 4). This is a critical first step to determine the spin pumping and SML contributions to the total damping.

1. Ferromagnetic dead layer measurement

In inductive VNA-FMR measurements, the FM layer contributes a frequency-independent inductance to the S_{21} measurement according to [26,27]

$$L_{\text{FM}} = \frac{\mu_0 l d_{\text{FM}}}{4 W_{\text{wg}}} \eta^2(z, W_{\text{wg}}), \tag{1}$$

where μ_0 is the permeability of free space, l is the sample length along the CPW signal propagation direction, d_{FM} is the deposited FM thickness, W_{wg} is the CPW signal linewidth, and $\eta(z, W_{\text{wg}}) \equiv (2/\pi)\arctan(W_{\text{wg}}/2z)$ is the spacing loss, ranging from 0 to 1, due to a finite distance z between sample and

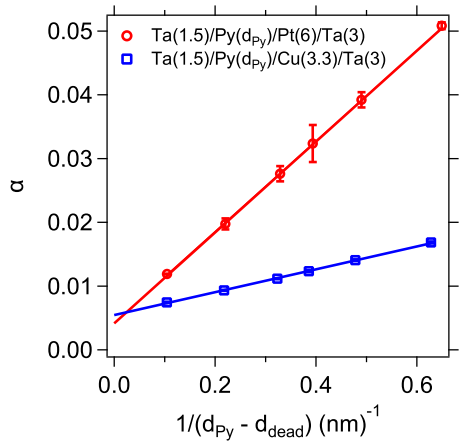

FIG. 4. Total Gilbert damping vs inverse effective FM thickness ($d_{\text{Py}} - d_{\text{dead}}$) for Py($d_{\text{Py}}$)/Pt(6) (circles) and Py(d_{Py})/Cu(3.3) (squares). Dead layer thickness is determined from Fig. 2.

CPW. When plotted vs d_{FM}, the $L_{\text{FM}} = 0$ intercept indicates the magnetic dead layer thickness. From the data in Fig. 2, we find $d_{\text{dead}} = (0.5 \pm 0.1)$ nm for Py/Pt samples. Also shown are the data for Py/Cu control samples, which exhibit a similar dead layer thickness of (0.41 ± 0.04) nm, suggesting that the Py dead layer exists primarily at the Ta/Py interface.

2. Determination of M_{s}

The effective magnetization M_{eff} as a function of applied microwave frequency is extracted from the FMR spectral fits and the Kittel FMR condition for magnetization oriented out of the film plane [28]:

$$H_{\text{res}} = \frac{\omega}{\gamma \mu_0} + M_{\text{eff}}, \tag{2}$$

where H_{res} is the center field of the resonant absorption line, ω is the applied microwave frequency, $\gamma = g\mu_{\text{B}}/\hbar$ is the gyromagnetic ratio, g is the spectroscopic g factor, μ_{B} is the Bohr magneton, and $\hbar$ is Planck's constant divided by 2π. Assuming the Py has no bulk anisotropy, M_{eff} is determined by the saturation magnetization M_{s} of the material, and the interfacial anisotropy energy K_{int} according to Ref. [29]:

$$\mu_0 M_{\text{eff}} = \mu_0 M_{\text{s}} - \frac{2K_{\text{int}}}{M_{\text{s}}}\left(\frac{1}{d_{\text{FM}} - d_{\text{dead}}}\right). \tag{3}$$

Therefore, a linear fit of M_{eff} vs inverse effective FM thickness (Fig. 3) provides a measurement of the saturation magnetization M_{s}. We find $\mu_0 M_{\text{s}} = (1.0671 \pm 0.0001)$ T, comparable to previous findings [29]. Similarly, for Py/Cu we find $\mu_0 M_{\text{s}} = (1.0453 \pm 0.0004)$ T.

3. Determination of intrinsic Gilbert damping constant

The total Gilbert damping due to intrinsic and interfacial contributions can be described by

$$\alpha = \alpha_{\text{int}} + G_{\text{eff}}^{\uparrow\downarrow}\left(\frac{\gamma \hbar^2}{2 M_{\text{s}} d_{\text{FM}} e^2}\right), \tag{4}$$

where e is the electron charge. M_{s} and d_{FM} for the Py layer are determined as described above. For the thin FM layers studied here, we can ignore the contribution from radiative damping [30]. When plotted vs $1/(d_{\text{Py}} - d_{\text{dead}})$, we can extract α_{int} as the infinite-thickness limit of the measured damping. We calculate the intercept of the data in Fig. 4 using linear regression in order to fix $\alpha_{\text{int}} = 0.0041 \pm 0.0001$, in good agreement with a previous systematic study of damping in magnetic alloys [29].

For the interfacial contribution to the damping [second term in Eq. (4)], the full model we use for the effective spin-mixing conductance $G_{\text{eff}}^{\uparrow\downarrow}$ includes contributions from spin pumping into Pt via the spin-mixing conductance $G_{\text{Py/Pt}}^{\uparrow\downarrow}$, spin pumping into the Ta seed layer via the spin-mixing conductance $G_{\text{Py/Ta}}^{\uparrow\downarrow}$, and spin-memory loss (SML). (In all instances where we invoke the spin-mixing conductance, it is to be understood that

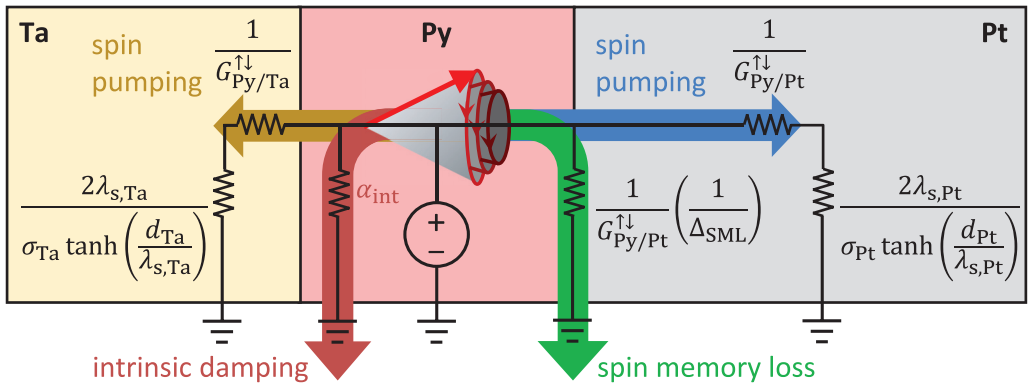

FIG. 5. Circuit model for angular momentum flow sourced by FMR excitation in Ta/Py/Pt trilayer. Spin current is drawn into parallel resistance channels provided by spin pumping into the Ta seed and Pt spin sink layers, as well as spin-memory loss.

we are only considering the real part of said quantity).

$$G^{\uparrow\downarrow}_{\text{eff}} = \frac{G^{\uparrow\downarrow}_{\text{Py/Pt}}}{1+\dfrac{2\lambda_{\text{s,Pt}}G^{\uparrow\downarrow}_{\text{Py/Pt}}}{\sigma_{\text{Pt}}(d_{\text{Pt}})\tanh\left(\dfrac{d_{\text{Pt}}}{\lambda_{\text{s,Pt}}}\right)}} + \frac{G^{\uparrow\downarrow}_{\text{Py/Ta}}}{1+\dfrac{2\lambda_{\text{s,Ta}}G^{\uparrow\downarrow}_{\text{Py/Ta}}}{\sigma_{\text{Ta}}(d_{\text{Ta}})\tanh\left(\dfrac{d_{\text{Ta}}}{\lambda_{\text{s,Ta}}}\right)}} + G^{\uparrow\downarrow}_{\text{Py/Pt}}\Delta_{\text{SML}}. \quad (5)$$

This model is depicted as a network of series and parallel conductance channels for the flow of angular momentum, treating FMR as an angular momentum potential source, as depicted in Fig. 5 (also see Ref. [31]). The first two terms of Eq. (5) represent spin pumping into the Pt and Ta layers, respectively. Within those layers, spin is pumped through series resistances set by the interfacial spin-mixing conductance, and thickness-dependent spin resistance (which accounts for the exponential spin accumulation profile in the NM layer, as a solution to the spin diffusion equation, subject to the boundary condition that no spin current can flow through the distant interface). The final term represents a spin-memory loss channel, where the phenomenological parameter Δ_{SML} can be arbitrarily large. By multiplying Eq. (5) by the bracketed term in Eq. (4), conductances are converted to the unitless damping parameters $\alpha_{\text{sp,Pt(Ta)}}$ [due to spin pumping into Pt (or Ta)] and α_{SML} (due to spin-memory loss).

Taken together, Eqs. (4) and (5) describe both the NM and FM thickness dependencies of the damping. As a part of our self-consistent fitting routine (described in Sec. III C), and using the previously determined value for α_{int}, we fit the Py thickness dependence of α simultaneously with the Pt thickness dependence [Fig. 8(b)], with $G^{\uparrow\downarrow}$ and Δ_{SML} as fit parameters. The result of that simultaneous fit is shown in Fig. 4. Also shown for comparison are damping data for the Py/Cu controls, which exhibit a drastically reduced spin pumping contribution (slope), and slightly increased intrinsic contribution ($\alpha_{\text{int}} = 0.0054 \pm 0.0001$).

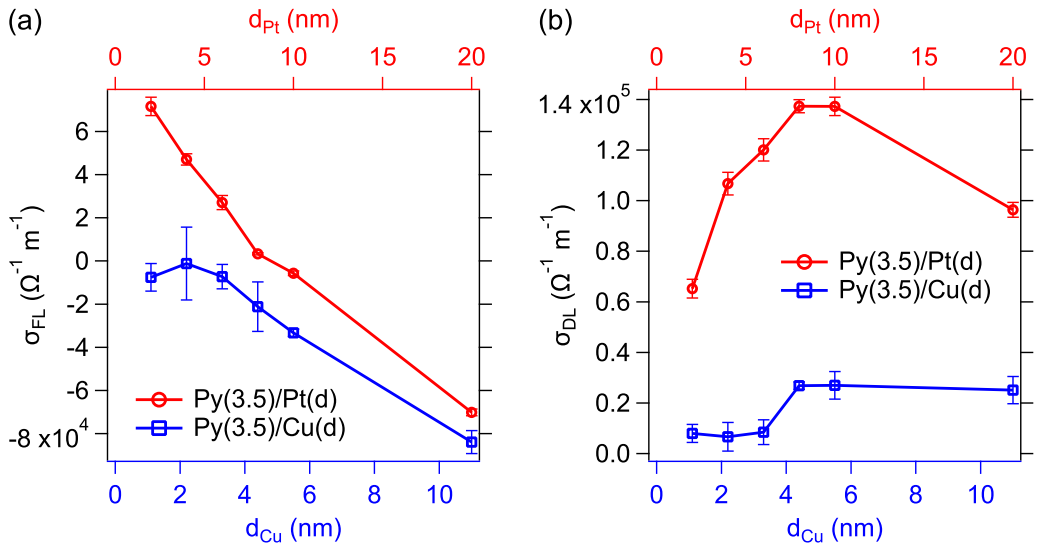

FIG. 6. Measured quantities for FL and DL conductivities, for both Pt and Cu control samples, extracted from complex inductance analysis of VNA-FMR data [26]. (a) σ_{FL} as a function of either Pt (top axis) or Cu thickness (bottom axis). Linear dependence on NM thickness at large thicknesses indicates dominance of the $\sigma^{\text{F}}_{\text{FL}}$ term. (b) Same as (a), but for σ_{DL}.

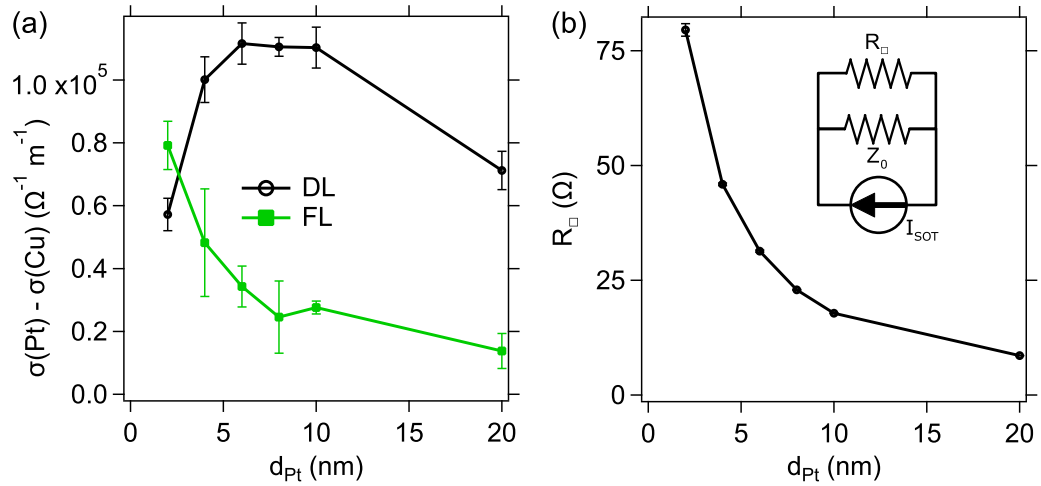

FIG. 7. (a) FL and DL iSOT conductivities, after subtraction of Cu control samples. (b) Measured sheet resistance of metallic layers, as a function of Pt thickness. Inset: the sample sheet resistance acts as a parallel shunting path to the signal generating component of I_{SOT}, which flows through the characteristic impedance Z_0 and $R_\square$.

B. Pt thickness series

For samples where the Pt thickness is varied, the measured values for σ_{FL} and σ_{DL}—extracted from our quantitative VNA-FMR complex amplitude analysis [26]—are shown as a function of NM thickness in Fig. 6. Two corrections must be made to these values in order to extract the iSOT due to Pt. First, we subtract the values for σ_{FL} and σ_{DL} obtained from the Cu control samples (blue squares) from those of the Pt samples (red circles). Since we used Cu thicknesses to match the sheet resistance of the Pt samples, this removes the Faraday contribution. This subtraction also removes any FL or DL iSOT due to the Ta seed and capping layers. While we do not completely understand the Cu thickness dependence of σ_{DL}, the DL signal is essentially eliminated for Py in isolation, without seed or capping layers, which suggests details of the iSOT from cap and/or seed layers are responsible for the peculiar behavior (see discussion and measurements in Sec. III D). In Fig. 7(a), σ_{FL} and σ_{DL} after Cu reference subtraction are plotted.

Second, we correct for shunting effects of the iSOT currents. The data of Fig. 7(a) attenuate as the Pt thickness is increased. This is attributed to the decreasing sheet resistance of the metallic stack, which effectively shunts the ac iSOT currents, therefore producing a weaker inductive response. This is functionally similar to the current divider effect observed in dc voltage iSHE spin pumping experiments [8,9,32,33]. However, in our ac iSOT experiments with the sample placed on a CPW with characteristic impedance of 50Ω, the sample sheet resistance acts as a shunt path in parallel with the CPW characteristic impedance [inset of Fig. 7(b)]. We therefore multiply the σ_{FL} and σ_{DL} results of Fig. 7(a) by the shunt factor $(1 + Z_0/R_\square)$, where $R_\square$ is the measured sheet resistance of the multilayer stack [Fig. 7(b)].

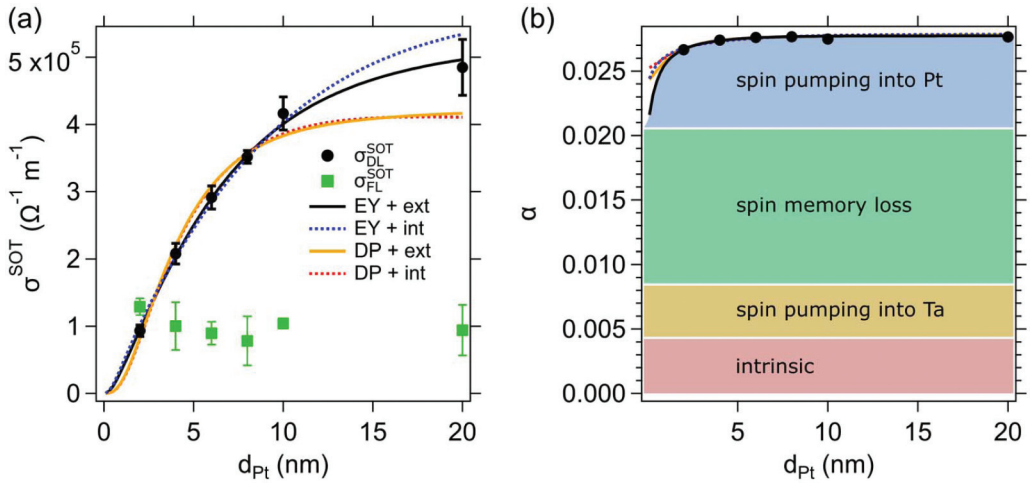

FIG. 8. (a) Final values for $\sigma_{\mathrm{DL}}^{\mathrm{SOT}}$ and $\sigma_{\mathrm{FL}}^{\mathrm{SOT}}$ for Py(3.5)/Pt(d_{Pt}). The FL torque remains constant over the range of studied thicknesses, whereas the DL torque increases with a characteristic length scale. (b) Gilbert damping for the same sample series (error bars are smaller than symbols). Color coding indicates different contributions to the Gilbert damping. Both the SOT conductivity and damping are fit to four different models, where spin relaxation is either EY or DP, and the spin Hall effect arises from intrinsic (int) or extrinsic (ext) processes. In both cases EY + ext (black solid line) provides the best fit, as determined by a χ^2 analysis.

After application of the shunting correction, the final results for σ_{FL}^{SOT} and σ_{DL}^{SOT} are presented in Fig. 8(a). These results are shown adjacent to the dependence of the measured Gilbert damping parameter α on Pt thickness in Fig. 8(b) to compare their evolution with d_{Pt}. The DL conductivity increases monotonically with Pt thickness. Meanwhile, the FL conductivity remains more or less constant, consistent with the presumption of an interfacial source of spin-charge conversion such as iREE, where additional Pt beyond 2 nm does not increase the charge signal further. From Fig. 8(b), it is clear that if the enhanced damping [second term in Eq. (4)] were ascribed entirely to spin pumping into the Pt, the length scale necessary to capture the rapid increase in α above the intrinsic value must be much shorter than the length scale over which σ_{DL}^{SOT} is seen to increase in Fig. 8(a). In other words, using only the data for Pt-thickness dependence of damping [Fig. 8(b)], it is impossible to separate the different contributions to $G_{eff}^{\uparrow\downarrow}$. Several other groups have observed this apparent discrepancy when comparing damping with dc voltages measured by iSHE [8–10]. In this work, we are able to resolve the discrepancy through a self-consistent fit of both the damping data and σ_{DL}^{SOT} vs Pt thickness.

Although we measure only a 3% enhancement of damping as d_{Pt} increases from 2 to 20 nm, given the high signal-to-noise ratio of the damping data, it can be fit with Eqs. (4) and (5) by use of the same spin diffusion length that describes the behavior of σ_{DL}^{SOT}, as discussed in detail later. Because of the better dynamic range of the σ_{DL}^{SOT} data, we use it as the basis for establishing λ_s by fitting with a model provided by Haney *et al.* [34]:

$$\sigma_{DL}^{SOT} = \sigma_{SH}\left\{\frac{(1-e^{-d_{NM}/\lambda_s})^2}{(1+e^{-2d_{NM}/\lambda_s})}\frac{|\tilde{G}^{\uparrow\downarrow}|^2+\mathrm{Re}(\tilde{G}^{\uparrow\downarrow})\tanh^2\left(\frac{d_{NM}}{\lambda_s}\right)}{|\tilde{G}^{\uparrow\downarrow}|^2+2\mathrm{Re}(\tilde{G}^{\uparrow\downarrow})\tanh^2\left(\frac{d_{NM}}{\lambda_s}\right)+\tanh^4\left(\frac{d_{NM}}{\lambda_s}\right)}\right\}\epsilon, \tag{6}$$

where $\tilde{G}^{\uparrow\downarrow} = G^{\uparrow\downarrow}2\lambda_s\tanh(d_{NM}/\lambda_s)/\sigma$, σ represents the NM charge conductivity, and $\epsilon \equiv \alpha_{sp,Pt}/(\alpha_{sp,Pt}+\alpha_{SML})$ represents the fraction of spin current pumped out of the FM that is available for spin-charge conversion in the Pt layer, as determined by the the spin current divider model applied to the first and last terms of Eq. (5).

C. Self-consistent fit routine of damping and SOT

To perform the self-consistent fits of σ_{DL}^{SOT} and α, an initial fit of σ_{DL}^{SOT} is performed to extract the Pt spin diffusion length $\lambda_{s,Pt}$. This is then used as a fixed parameter in Eqs. (4) and (5) when fitting α. With this constraint on $\lambda_{s,Pt}$, the Pt and Py thickness series [Figs. 8(b) and 5, respectively] are fitted simultaneously with Eqs. (4) and (5) to determine $G_{Py/Pt}^{\uparrow\downarrow}$ and Δ_{SML}. These are then put back into Eq. (6) to refit σ_{DL}^{SOT} and extract refined values for σ_{SH} and $\lambda_{s,Pt}$. This process is iterated until the change in fit parameters is less than 0.01%.

Our self-consistent data analysis is tantamount to enforcing Onsager reciprocity on the spin-to-charge interconversion processes of spin pumping and spin torque [35]. If the enhanced damping of Fig. 8(b) were ascribed purely to spin pumping, it would imply that the Pt already draws a maximum amount of spin current from the precessing FM at thicknesses of only $\approx$2 nm. By contrast, a dampinglike torque conductivity that continues to increase for thicknesses up to 10 nm [Fig. 8(a)] suggests that the Pt layer can continue to generate (or draw) increasingly larger spin current for thicknesses well beyond 2 nm. The use of unequal length scales to describe diffusive spin current flow due to spin pumping and spin-orbit torque generation would violate the reciprocity of spin-to-charge interconversion.

Equations (5) and (6) can be used either with an Elliott-Yafet (EY) [36,37] or Dyakonov-Perel (DP) [38] spin-relaxation model. In the EY case, the spin diffusion length is a function of the charge conductivity: $\lambda_s[\sigma(d_{NM})] = [\sigma(d_{NM})/\sigma_{bulk}]\lambda_s^{max}$. The thickness-dependent conductivity and bulk conductivity σ_{bulk} are both determined by four-probe resistance measurements (see Sec. V A). By contrast, for DP spin relaxation, λ_s is independent of charge conductivity [13]. Additionally, the spin Hall conductivity in Eq. (6) can be attributed to intrinsic or extrinsic SOC. For intrinsic spin Hall, σ_{SH} is independent of charge conductivity, while for extrinsic SHE, $\sigma_{SH}(d_{NM}) = \theta_{SH}\sigma(d_{NM})$, where θ_{SH} is fixed. We stress that the models we are considering here assume a spatially constant spin diffusion length and conductivity, although their values are adjusted for each value of the Pt thickness when appropriate for the model under consideration. It has been argued [17] that a more realistic approach is to allow for a spatial dependence of both λ_s and σ_{SH}. As pointed out by the authors of Ref. [17], this approach nevertheless assumes EY-type scattering, since it relies on the linear scaling of spin diffusion length with Pt conductivity. While it is often assumed that EY effects should dominate in centrosymmetric materials, we see no reason to bias the data fitting process. The symmetry breaking at the Pt interface by itself nullifies any arguments that DP effects should be ignored. Fits using the four combinations of these models (EY or DP and intrinsic or extrinsic SHE) are shown in Fig. 8, with results collected in Table I. To distinguish between the quality of fit for the different models, we utilize a χ^2 test.

The χ^2 values for each fit of the SOT and damping data is calculated as $\chi^2 \equiv \sum_i^n (y_i - f_i)^2/\sigma_i^2$, where y_i is the measured value, f_i is the calculated value based on the fit model, and σ_i^2 is the measured variance, for each of n measurements. Results are shown in Table II. Using the cumulative distribution function (CDF) of a χ^2 distribution for each fit, with $\nu = n - p$ degrees of freedom, and p fit parameters, we also calculate the joint probability with which we can reject the null hypothesis in which there is no relationship between our measurements and

TABLE I. Comparison of fitted values for $G^{\uparrow\downarrow}$, ϵ, λ_s, σ_{SH}, and θ_{SH} using different models for the source of spin relaxation (EY or DP) and SHE (intrinsic or extrinsic). For EY models, the spin diffusion length is reported as λ_s^{max}.

Fit model	$G^{\uparrow\downarrow}(\times 10^{14}\ \Omega^{-1}\,m^{-2})$	$\epsilon = \frac{\alpha_{sp,Pt}}{(\alpha_{sp,Pt}+\alpha_{SML})}$	λ_s (nm)	$\sigma_{SH}(\times 10^6\ \Omega^{-1}\,m^{-1})$	$\theta_{SH} = \frac{\sigma_{SH}}{\sigma_{Pt}}$
EY + ext	13 ± 2	(0.37 ± 0.06)	4.2 ± 0.1	2.36 ± 0.04	0.387 ± 0.008
EY + int	5.6 ± 0.1	(0.20 ± 0.04)	6.7 ± 0.3	5.3 ± 0.3	0.86 ± 0.05
DP + ext	3.0 ± 0.3	(0.19 ± 0.02)	2.5 ± 0.2	11.6 ± 0.4	1.91 ± 0.06
DP + int	2.2 ± 0.3	(0.13 ± 0.02)	3.7 ± 0.3	13.5 ± 0.5	2.22 ± 0.08

the given model. The CDF is determined by

$$\mathrm{CDF}(\chi^2) = \int_0^{\chi^2} \frac{t^{\nu/2-1}e^{-t/2}}{\Gamma(\nu/2)2^{\nu/2}}dt, \tag{7}$$

where $\Gamma(x) = (x-1)!$. The joint probability is calculated as the product of $[1 - \mathrm{CDF}(\chi^2)]$ for the two fits. The EY/extrinsic model provides the highest confidence that we can reject the null hypothesis. Because this analysis reveals EY spin relaxation with extrinsic SHE as the best fit to our data, we focus on the fitted parameters from that model combination in the discussion below.

With regard to the interpretation of the χ^2 analysis presented here, the high value for the joint probability in the case of the EY/extrinsic model does not automatically justify exclusion of alternative models. Indeed, it merely estimates that the probability of obtaining another data set with a smaller fitting residue is on the order of 11%. It is not the case that such a low probability means that the EY/extrinsic model is the only correct model. The joint probabilities for the other three simple models considered here, while not as favorable, do not disqualify those models from plausibility. Furthermore, it is likely that the sample and material properties matter significantly, as in the recent observation of DP-type spin relaxation for single-crystal Pt [39].

By choosing to enforce reciprocity, we find that the fraction of spin current absorbed by the Pt layer (which produces the dampinglike ac charge currents) reaches a maximum of $(37 \pm 6)\%$ for the thickest Pt layers. This is comparable to previous findings of large SML at Co/Pt interfaces [40] and Pt/Cu interfaces [19]. The different contributions to the total measured damping are represented as shaded areas in Fig. 8(b), with a color code to match Fig. 5. Note that only the contribution from spin pumping into Pt is Pt-thickness dependent. The self-consistent fit also results in a spin diffusion of length of $\lambda_{s,Pt}^{max} = (4.2 \pm 0.1)$ nm, $G^{\uparrow\downarrow} = (1.3 \pm 0.2) \times 10^{15}\ \Omega^{-1}\,m^{-2}$, which is in good agreement with the maximum theoretical value for Pt of $G^{\uparrow\downarrow} = 1.07 \times 10^{15}\ \Omega^{-1}\,m^{-2}$ [41], given the estimated error, and $\sigma_{SH}^{bulk} = (2.36 \pm 0.04) \times 10^6\ \Omega^{-1}\,m^{-1}$. This corresponds to a spin Hall angle of 0.387 ± 0.008. While this θ_{SH} is among the largest reported for Pt [42,43], it is a necessary logical conclusion that with less spin current driven into the NM (on account of SML), a larger spin-to-charge conversion efficiency is required to fit the data than would be otherwise obtained if the SML were negligible. We furthermore stress that the phenomenological value for σ_{DL}^{SOT} [the asymptotic value in Fig. 8(a)] is comparable to that measured with other techniques [$5.8 \times 10^5\ \Omega^{-1}\,m^{-1}$ for $AlO_x(2)/Co(0.6)/Pt(3)$ [7], $4.8 \times 10^5\ \Omega^{-1}\,m^{-1}$ for $Ta(2)/Pt(4)/Co_{50}Fe_{50}(0.5)/MgO(2)/Ta(1)$ [43], and $\approx 2.5 \times 10^5\ \Omega^{-1}\,m^{-1}$ for $Ta(1)/Pt(d_{Pt})/Co(1)/MgO(2)/Ta(1)$ [17]]. This indicates consistency of the SOC strength of the Pt layers in each of these experiments, and stresses the importance of characterizing spin loss mechanisms to optimize SOT for magnetic switching.

We previously reported that the best fits for spin pumping data in similar multilayer stacks were provided by a model that assumed a DP spin-relaxation mechanism [13]. However, in the previous work, the spin pumping data that was fitted included very small Pt thicknesses of 0.5, 1, and 1.5 nm. It is now understood that the spin transport properties of such thin Pt in direct contact with a FM layer are dominated by proximity polarization effects [15]. In addition, it has also been predicted that an interfacial Rashba effect at the FM/NM interface naturally leads to spin-memory loss and a rapid, quasilinear increase in the damping with increasing NM thickness for the first nanometer [20]. While the details of the models used to fit the spin pumping data in Refs. [13,15] are sufficiently different to make direct comparison difficult, it is incontrovertible that the immediate contact of the Pt and Py layers in our samples leads to some degree of spin polarization in the Pt over the first 0.5 to 1.5 nm, motivating us to now exclude data at such small thicknesses from the fits to Eqs. (4) and (5). Even though those data are excluded, we are now able to ascertain fits of the spin transport parameters because of our ability to simultaneously fit the spin pumping data and the SOT data, thereby allowing us to directly observe the important role of spin-memory loss with a much higher degree of accuracy than was achieved in Ref. [13].

Our finding that the data are best fit with an extrinsic SHE model is somewhat surprising, given that it conflicts with some previous experimental work [17] and theoretical expectations [44]. Qualitatively, both intrinsic and extrinsic SHE models are seen to describe the data quite well, given that the fit parameters can adjust to compensate for differences in the models, as is seen by the various fits in Fig. 8(a). Nevertheless, the χ^2 analysis makes a clear distinction. Finally,

TABLE II. χ^2 values for SOT fit [Fig. 8(a)] and simultaneous damping fit [Figs. 8(b) and 5]. The joint probability represents the confidence with which we can reject the null hypothesis.

Fit model	χ^2 (SOT)	χ^2 (damping)	Joint probability
EY + ext	0.668	3.696	0.89
EY + int	3.123	12.032	0.11
DP + ext	8.149	5.715	0.07
DP + int	8.819	6.101	0.05

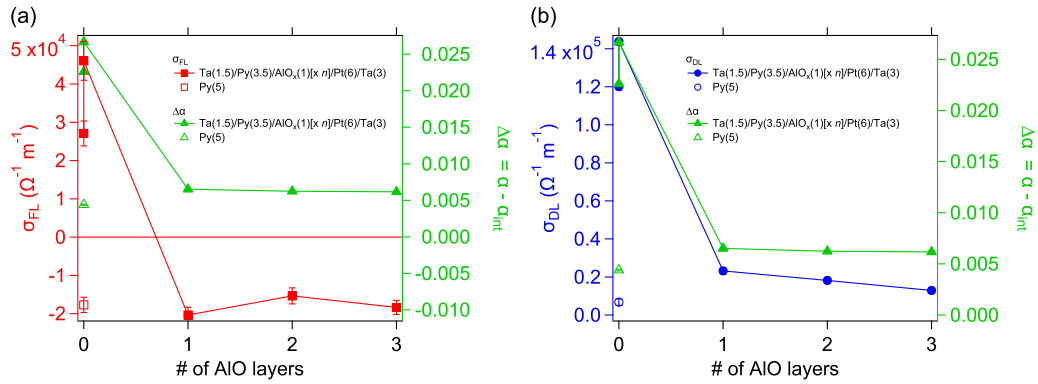

FIG. 9. (a) FL conductivity for samples with AlO_x $[\times n]$ (where $n = 0$, 1, 2, or 3) blocking layers inserted between Py(3.5) and Pt(6) (squares, left axis). Change in damping $\Delta\alpha$ relative to intrinsic value shown on right axis (triangles). (b) Same as (a), but for DL conductivity (circles, left axis). Damping values (right axis) are identical to (a) and repeated for comparison purposes. Note that Py(3.5)/Pt(6) (direct contact) was regrown and remeasured as a part of the AlO_x series (duplicate data points for zero AlO_x repeats). The lower data point for both σ_{FL} and σ_{DL} at zero AlO_x layers is that from the main text.

the value for σ_{SH} determined here is more than five times larger than the 0 K prediction by Guo *et al.* (using their result of $\sigma_{xy} = 2.2 \times 10^5(\hbar/e)\ \Omega^{-1}m^{-1}$, and setting $\sigma_{SH} = 2\sigma_{xy}$ to account for the total spin current due to both up and down spins [44]). This implies that the extrinsic effect dominates in our sputtered thin-film systems where interfaces and crystal defects likely play a major role in determining the spin-orbit physics [45].

It is possible that some amount of intrinsic SHE is present in addition to the extrinsic effect, as discussed by Sagasta, *et al.* [3]. In that work, the authors show that the total effective spin Hall conductivity σ_{SH}^{eff} can be described by

$$\sigma_{SH}^{eff} = \sigma_{SH}^{int} + \theta_{SH}^{ext}\sigma_{Pt}, \tag{8}$$

where σ_{SH}^{int} is the intrinsic spin Hall conductivity, and the second term describes the extrinsic effect as we have modeled it here. The Pt conductivities studied here (from $\approx 3 \times 10^6\ \Omega^{-1}\,m^{-1}$ to $6 \times 10^6\ \Omega^{-1}\,m^{-1}$) fall within the transition from intrinsic to extrinsic regimes, as described in Ref. [3]. Therefore, depending on the details of the spin and momentum scattering that govern θ_{SH}, the extrinsic term in Eq. (8) can easily be the dominant effect. Furthermore, we see no evidence of a large interfacial source of spin Hall conductivity, as in Ref. [46], which would manifest as a nonzero intercept of σ_{DL}^{SOT} in the limit of $d_{Pt} \to 0$.

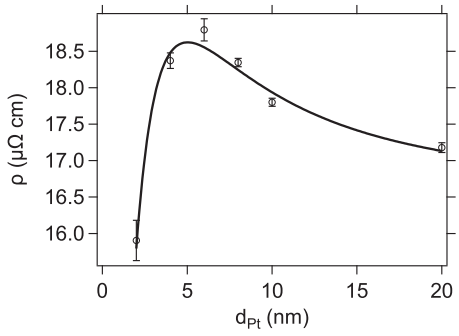

FIG. 10. Thickness-dependent resistivity, measured for substrate/Ta(1.5)/Py(3.5)/Pt(d_{Pt})/Ta(3) as a function of Pt thickness.

D. Isolating the normal-metal layer contribution to sample inductance

To better understand the influence of the normal-metal layers (Ta seed, Pt or Cu spin sink, and Ta cap) on the perturbative inductance—and hence, the extracted FL and DL conductivities—that the sample contributes to a VNA-FMR measurement, we measured several control samples. First, we inserted an AlO_x layer between the Py and the Pt in order to block spin pumping into the Pt [47]. To do so, 1 nm of Al was sputter deposited onto the Py and subsequently oxidized for 10 min under 5 Torr of O_2. The AlO_x layer deposition and oxidation steps were repeated one, two, or three times, to ensure complete blocking of spin pumping. As can be seen in Fig. 9(b), the AlO_x layers effectively reduce the damping by blocking spin pumping. This reduction correlates strongly with a reduction in σ_{DL}, confirming its signature as the dampinglike conductivity.

By contrast, σ_{FL} actually changes sign with the introduction of the AlO_x layers [Fig. 9(a)]. The contribution to σ_{FL} by Faraday-type pickup in the Pt cannot be eliminated by the AlO_x barrier, since the Pt can still inductively couple to the precessing magnetization in the Py. The Faraday contribution clearly adds a negative contribution to σ_{FL}, as σ_{FL} becomes increasingly negative with thicker Pt and Cu layers, as in Fig. 6(a). Therefore, the AlO_x barrier might eliminate the σ_{FL}^{SOT} contribution at the top Py interface. Nevertheless, even for Py deposited directly on SiO_2 (open square symbol), there remains a negative total σ_{FL}, perhaps due to the interface asymmetry that remains between the top and bottom Py interfaces.

The control samples also elucidate the impact of the Ta layers on our measurements. We note that Eq. (5) does not explicitly include SML at the Ta interface. Using the data from Fig. 9(b), we find that this simplification is justified. For these samples, we measured a total damping of $\alpha_{tot} = 0.0104 \pm 0.0002$. If we set $G_{Py/Ta}^{\uparrow\downarrow} = 7.4 \times 10^{14}\ \Omega^{-1}\,m^{-2}$ (the Sharvin value for Ta [41]), and use our measured conductivity of $\sigma_{Ta} = (8.91 \pm 0.02) \times 10^5\ \Omega^{-1}\,m^{-1}$, we obtain $\alpha_{sp,Ta} = 0.004$ [the amount depicted in Fig. 8(b)]. Therefore, when damping pathways into the Pt are blocked, the intrinsic damping plus spin pumping into the Ta accounts for all but 0.0023 of the total

damping. Assigning this small amount of excess damping to SML at the Ta interface would reduce the contribution of SML at the Pt interface by less than 20% and the values for spin Hall conductivity and spin Hall angle in Pt by only 10%.

Finally, we fabricated samples without any seed or capping layers. For Py(5) deposited directly onto SiO_2, σ_{DL} is only 5% of its value for Py(3.5)/Pt(6) [see the open circle data point in Fig. 9(b)]. The residual damping (beyond the intrinsic value) and dampinglike conductivity for this sample could stem from the oxidized top surface or interfacial asymmetries, as well as less-than-optimal Py crystal structure, since no Ta seed layer was used.

In the cases of both σ_{FL} and σ_{DL}, some residual signal remains even when spin pumping into the Pt is effectively blocked, or the seed and capping layers are eliminated entirely. Therefore, it is not surprising that even for our control samples in which Pt is replaced with Cu (with its weak spin-orbit interaction), some weak sources of spin-to-charge conversion (interfacial or otherwise) persist.

IV. CONCLUSION

To summarize, by use of simultaneously acquired damping and iSOT data, we are able to properly assign the portions of damping enhancement incurred by a FM/NM bilayer due to the parallel channels of SML and spin pumping into the NM. These results suggest that Pt is indeed a promising material for spintronic applications. Our data also validate previous suggestions that interface engineering will be crucial for the optimization of SOT in multilayer systems [10,40,42,43].

ACKNOWLEDGMENT

Contributions to this article by workers at NIST, an agency of the US Government, are not subject to US copyright.

APPENDIX: Pt THICKNESS-DEPENDENT RESISTIVITY

To extract the Pt contribution to the total measured stack resistance, we have developed a reasonable empirical model for the metallic multilayer stack to account for different conductivities in the bulk and at the metal interfaces. In this model, the interfacial conductivity σ_{int} at the Py/Pt interfaces decays exponentially to the Pt bulk value, $1/\rho_0$, with increasing distance from the interface. Position-dependent conductivity through the Pt thickness can therefore be approximated as the sum of bulk and interfacial contributions:

$$\sigma(z) = \frac{1}{\rho_0}\left[1 - \exp\left(\frac{-z}{\sigma_{int}\rho_0\lambda}\right)\right] + \sigma_{int}\exp\left(\frac{-z}{\sigma_{int}\rho_0\lambda}\right), \tag{A1}$$

where ρ_0 is the bulk resistivity, σ_{int} is the interfacial conductivity, and λ is the bulk mean free path. The length scale $\sigma_{int}\rho_0\lambda$ describes the effective thickness over which the conductivity is determined by σ_{int}. When $\sigma(z)$ is integrated over the Pt thickness from $z = 0$ to $z = d_{Pt}$, we obtain a final result for thickness-dependent resistivity:

$$\rho(d_{Pt}) = \frac{\rho_0}{\left[1 + \left(\frac{\sigma_{int}\rho_0\lambda}{d_{Pt}}\right)(\rho_0\sigma_{int} - 1)\left[1 - \exp\left(\frac{-d_{Pt}}{\sigma_{int}\rho_0\lambda}\right)\right] + \left(\frac{1}{R_{other}}\right)\left(\frac{\rho_0}{d_{Pt}}\right)\right]}, \tag{A2}$$

where R_{other} represents the sheet resistances of any fixed-thickness metallic layers (here, Py and Ta). We use a calculated mean free path for our samples (12.79 nm) by scaling a literature value [48] (13 nm) by the ratio of our measured bulk resistivity to the literature value for bulk resistivity. From the fit in Fig. 10, we obtain $\sigma_{int} = (1.29 \pm 0.09) \times 10^6\ \Omega^{-1}\,m^{-1}$, $\rho_0 = (1.63 \pm 0.01) \times 10^{-7}\ \Omega\,m$, and $R_{other} = (138 \pm 3)\ \Omega$. These values are used to obtain the thickness-dependent conductivity of the Pt layer, required in Eqs. (5) and (6).

The motivation for this highly simplified resistivity model is the widely accepted claim that the proportionality of thin-film resistivity on reciprocal film thickness is the result of diffuse interface scattering (see Ref. [17], and references therein). The model presented here provides a reasonable fit to our resistivity data with a minimum of free fitting parameters, but with due regard for the most important physical effects that affect thin-film conductivity. While our model does not account for the many details contained in the more rigorous Fuchs-Sondheimer model, such as scattering at grain boundaries, it is self-consistent in its application of a position-dependent conductivity that necessarily increases monotonically with increasing distance from the interface in the case of a semi-infinite film.

In Ref. [17], the authors model the Pt film as a series of adjacent "slices" of thickness l^i with a locally defined resistivity ρ^i (for the ith slice). While this model has intuitive appeal for capturing the commonly observed dependence of thin-film resistivity with layer thickness, it nevertheless requires an assumption of locality in which the mean free path is less than the thickness of the individual slices. The veracity of this assumption is tenuous, given that the bulk mean free path for Pt is 13 nm according to Fischer *et al.* [48]. Instead, the locally enhanced scattering process at the film interfaces is best modeled as a sum of interfacial and bulk contributions to the conductance (i.e., series conductances, as captured by Eq. (A1), in contrast to the series resistances of Ref. [17]).

[1] E. Saitoh, M. Ueda, H. Miyajima, and G. Tatara, Appl. Phys. Lett. **88**, 182509 (2006).

[2] S. O. Valenzuela and M. Tinkham, Nature (London) **442**, 176 (2006).

[3] E. Sagasta, Y. Omori, M. Isasa, M. Gradhand, L. E. Hueso, Y. Niimi, Y. C. Otani, and F. Casanova, Phys. Rev. B **94**, 060412(R) (2016).

[4] D. Qu, S. Y. Huang, B. F. Miao, S. X. Huang, and C. L. Chien, Phys. Rev. B **89**, 140407 (2014).

[5] H. Nakayama, M. Althammer, Y.-T. Chen, K. Uchida, Y. Kajiwara, D. Kikuchi, T. Ohtani, S. Geprägs, M. Opel, S. Takahashi, R. Gross, G. E. W. Bauer, S. T. B. Goennenwein, and E. Saitoh, Phys. Rev. Lett. **110**, 206601 (2013).

[6] L. Liu, T. Moriyama, D. C. Ralph, and R. A. Buhrman, Phys. Rev. Lett. **106**, 036601 (2011).

[7] K. Garello, I. M. Miron, C. O. Avci, F. Freimuth, Y. Mokrousov, S. Blügel, S. Auffret, O. Boulle, G. Gaudin, and P. Gambardella, Nat. Nanotechnol. **8**, 587 (2013).

[8] H. Nakayama, K. Ando, K. Harii, T. Yoshino, R. Takahashi, Y. Kajiwara, K. Uchida, Y. Fujikawa, and E. Saitoh, Phys. Rev. B **85**, 144408 (2012).

[9] Z. Feng, J. Hu, L. Sun, B. You, D. Wu, J. Du, W. Zhang, A. Hu, Y. Yang, D. M. Tang, B. S. Zhang, and H. F. Ding, Phys. Rev. B **85**, 214423 (2012).

[10] J.-C. Rojas-Sánchez, N. Reyren, P. Laczkowski, W. Savero, J.-P. Attané, C. Deranlot, M. Jamet, J.-M. George, L. Vila, and H. Jaffrès, Phys. Rev. Lett. **112**, 106602 (2014).

[11] T. Nan, S. Emori, C. T. Boone, X. Wang, T. M. Oxholm, J. G. Jones, B. M. Howe, G. J. Brown, and N. X. Sun, Phys. Rev. B **91**, 214416 (2015).

[12] A. Conca, B. Heinz, M. R. Schweizer, S. Keller, E. T. Papaioannou, and B. Hillebrands, Phys. Rev. B **95**, 174426 (2017).

[13] C. T. Boone, J. M. Shaw, H. T. Nembach, and T. J. Silva, J. Appl. Phys. **117**, 223910 (2015).

[14] S. Azzawi, A. Ganguly, M. Tokaç, R. M. Rowan-Robinson, J. Sinha, A. T. Hindmarch, A. Barman, and D. Atkinson, Phys. Rev. B **93**, 054402 (2016).

[15] M. Caminale, A. Ghosh, S. Auffret, U. Ebels, K. Ollefs, F. Wilhelm, A. Rogalev, and W. E. Bailey, Phys. Rev. B **94**, 014414 (2016).

[16] A. Azevedo, L. H. Vilela-Leão, R. L. Rodríguez-Suárez, A. F. Lacerda Santos, and S. M. Rezende, Phys. Rev. B **83**, 144402 (2011).

[17] M.-H. Nguyen, D. C. Ralph, and R. A. Buhrman, Phys. Rev. Lett. **116**, 126601 (2016).

[18] C. Stamm, C. Murer, M. Berritta, J. Feng, M. Gabureac, P. M. Oppeneer, and P. Gambardella, Phys. Rev. Lett. **119**, 087203 (2017).

[19] H. Kurt, R. Loloee, K. Eid, W. P. Pratt, and J. Bass, Appl. Phys. Lett. **81**, 4787 (2002).

[20] K. Chen and S. Zhang, Phys. Rev. Lett. **114**, 126602 (2015).

[21] S. S. Kalarickal, P. Krivosik, M. Wu, C. E. Patton, M. L. Schneider, P. Kabos, T. J. Silva, and J. P. Nibarger, J. Appl. Phys. **99**, 093909 (2006).

[22] Y. Tserkovnyak, A. Brataas, and G. E. W. Bauer, Phys. Rev. Lett. **88**, 117601 (2002).

[23] S. Mizukami, Y. Ando, and T. Miyazaki, Phys. Rev. B **66**, 104413 (2002).

[24] B. Heinrich, G. Woltersdorf, R. Urban, and E. Simanek, J. Appl. Phys. **93**, 7545 (2003).

[25] M. A. W. Schoen, J. Lucassen, H. T. Nembach, T. J. Silva, B. Koopmans, C. H. Back, and J. M. Shaw, Phys. Rev. B **95**, 134410 (2017).

[26] A. J. Berger, E. R. J. Edwards, H. T. Nembach, A. D. Karenowska, M. Weiler, and T. J. Silva, Phys. Rev. B **97**, 094407 (2018).

[27] T. J. Silva, H. T. Nembach, J. M. Shaw, B. Doyle, K. Oguz, K. O'Brien, and M. Doczy, in *Metrology and Diagnostic Techniques for Nanoelectronics*, edited by Z. Ma and D. G. Seiler (Pan Stanford Publishing Pte. Ltd., Singapore, 2016).

[28] C. Kittel, *Introduction to Solid State Physics*, 8th ed. (Wiley, New York, 2004).

[29] M. A. W. Schoen, J. Lucassen, H. T. Nembach, B. Koopmans, T. J. Silva, C. H. Back, and J. M. Shaw, Phys. Rev. B **95**, 134411 (2017).

[30] M. A. W. Schoen, J. M. Shaw, H. T. Nembach, M. Weiler, and T. J. Silva, Phys. Rev. B **92**, 184417 (2015).

[31] K. Roy, Phys. Rev. B **96**, 174432 (2017).

[32] H. J. Jiao and G. E. W. Bauer, Phys. Rev. Lett. **110**, 217602 (2013).

[33] H. L. Wang, C. H. Du, Y. Pu, R. Adur, P. C. Hammel, and F. Y. Yang, Phys. Rev. Lett. **112**, 197201 (2014).

[34] P. M. Haney, H.-W. Lee, K.-J. Lee, A. Manchon, and M. D. Stiles, Phys. Rev. B **87**, 174411 (2013).

[35] A. Brataas, Y. Tserkovnyak, G. E. W. Bauer, and P. J. Kelly, *Spin Current* (Oxford University Press, Oxford, 2012).

[36] R. J. Elliott, Phys. Rev. **96**, 266 (1954).

[37] Y. Yafet, Phys. Lett. A **98**, 287 (1983).

[38] M. I. Dyakonov and V. I. Perel, Sov. Phys. Solid State **13**, 3023 (1972).

[39] J. Ryu, M. Kohda, and J. Nitta, Phys. Rev. Lett. **116**, 256802 (2016).

[40] H. Y. T. Nguyen, W. P. Pratt, and J. Bass, J. Magn. Magn. Mater. **361**, 30 (2014).

[41] Y. Liu, Z. Yuan, R. J. H. Wesselink, A. A. Starikov, and P. J. Kelly, Phys. Rev. Lett. **113**, 207202 (2014).

[42] W. Zhang, W. Han, X. Jiang, S.-H. Yang, and S. S. P. Parkin, Nat. Phys. **11**, 496 (2015).

[43] C.-F. Pai, Y. Ou, L. H. Vilela-Leão, D. C. Ralph, and R. A. Buhrman, Phys. Rev. B **92**, 064426 (2015).

[44] G. Y. Guo, S. Murakami, T.-W. Chen, and N. Nagaosa, Phys. Rev. Lett. **100**, 096401 (2008).

[45] V. P. Amin and M. D. Stiles, Phys. Rev. B **94**, 104420 (2016).

[46] L. Wang, R. J. H. Wesselink, Y. Liu, Z. Yuan, K. Xia, and P. J. Kelly, Phys. Rev. Lett. **116**, 196602 (2016).

[47] B. L. Zink, M. Manno, L. O'Brien, J. Lotze, M. Weiler, D. Bassett, S. J. Mason, S. T. B. Goennenwein, M. Johnson, and C. Leighton, Phys. Rev. B **93**, 184401 (2016).

[48] G. Fischer, H. Hoffmann, and J. Vancea, Phys. Rev. B **22**, 6065 (1980).